Available online at www.sciencedirect.com
ScienceDirect
Journal of Power Sources 162 (2006) 400–414
JOURNAL OF POWER SOURCES
www.elsevier.com/locate/jpowsour

Model development for a SOFC button cell using H_2S as fuel

Dayadeep S. Monder, K. Nandakumar*, Karl T. Chuang

Chemical and Materials Engineering, University of Alberta, Edmonton, Alberta, Canada T6G 2G6

Received 6 June 2006; received in revised form 30 June 2006; accepted 4 July 2006
Available online 17 August 2006

Abstract

In this paper we present a hierarchy of models built to describe the overall performance of a single H_2S fuelled button cell solid oxide fuel cell (SOFC). The cell, used in the experimental studies of Liu et al. [M. Liu, G. Wei, J. Luo, A.R. Sanger, K.T. Chuang, Use of metal sulfides as anode catalysts in H_2S–air SOFCs, J. Electrochem. Soc. 150 (2003) 1025–1029], was a planar cell with a circular disc-like electrode assembly and the fuel and air flowing through a concentric cylindrical tube assembly. The goal is to model the electrochemical reaction coupled with mass transfer, fluid flow and current/voltage distribution in an yttria stabilized zirconia electrolyte fuel cell assembly operated between 750 and 850 °C. The models built range in complexity from an algebraic system of equations that calculates the activation, concentration and ohmic losses, to a two-dimensional finite element model that solves all the physics in the SOFC simultaneously. Kinetic parameters in these (progressively more comprehensive) models have been estimated and compared, leading hopefully to more accurate estimates for these parameters.

Keywords: SOFC; Modelling; H_2S; Finite element model; Parameter estimation

1. Introduction

Hydrogen sulfide (H_2S) is a by-product of the natural gas and the petrochemical industries. In addition to being toxic to most forms of life it is an unpleasant smelling air pollutant. The primary industrial process used to dispose off H_2S is the Claus process [1]. The Claus process converts the gaseous H_2S to sulfur, a solid at ordinary temperatures, using a fairly complicated multistage process that has high operating costs.

If H_2S can be used as fuel in a fuel cell, it can be disposed off in a much simpler process that generates high quality electrical energy. The earliest studies on the possibility of using H_2S in a fuel cell were conducted by Pujare et al. [2,3]. Since then a number of studies have been published on fuel cells running on H_2S [4–12]. These studies were experimental ones that evaluated different materials for the anode, anode catalysts, and electrolyte. While some work has been reported on using H_2S in fuel cells with proton conducting electrolytes [9–12], most studies have used oxide ion conducting electrolytes.

For SOFCs using H_2S as fuel, many different anode materials have been investigated including thiospinels [2,3], Pt [13,5], various metal sulfides [4,6,8], and lanthanum strontium vanadate (LSV) [7]. Although all of these studies present fuel cell performance data in the form of current density and or power density curves, the main goal of these studies was to find materials that lead to stable performance for H_2S fuel cells without degradation over time.

Among the more recent studies, a group at the University of Alberta, Liu et al. [6] and Wei et al. [8,14] have presented performance data for H_2S fuelled SOFCs using mixed sulfide (and mixed sulfide, metal and electrolyte composite) anodes. These data include current density curves at different temperatures and fuel and air flow-rates. Although some impedance data are given, these data are for complete cells and does not attempt to isolate anode processes from cathode processes. Another recent study from the Georgia Institute of Technology by Aguilar et al. [7] presents performance data at different temperatures from a SOFC using an LSV anode. This work also gives performance and impedance data at different fuel compositions to demonstrate the selectivity of the anode to H_2S in preference to H_2. Neither of these studies, however, pin down the reaction mechanism or give any kinetic parameters.

It is in the presence of such limited data and uncertainties about detailed mechanisms that we attempt to develop a mathematical modelling framework. Such models can still be useful in assessing the relative importance of transport versus reaction mechanisms.

* Corresponding author. Tel.: +1 780 492 5810; fax: +1 780 492 2881.
E-mail address: kumar.nandakumar@ualberta.ca (K. Nandakumar).

0378-7753/$ – see front matter © 2006 Elsevier B.V. All rights reserved.
doi:10.1016/j.jpowsour.2006.07.014

Nomenclature

a_k	activity of species k
$a_{k,\text{in}}$	activity of species k at inlet
c_j	integration constant for voltage profile in phase j
C_k	molar concentration of k (mole m^{-3})
C_t	total molar concentration (mole m^{-3})
$D_{\text{eff},k}$	effective diffusivity of component k (m^2 s^{-1})
$\tilde{D}_{ij}$	multicomponent composition dependent diffusivity of species i in species j (m^2 s^{-1})
D_{ik}	multicomponent Maxwell–Stefan diffusivity of species i in k (m^2 s^{-1})
$D_{K,k}$	Knudsen diffusivity for k (m^2 s^{-1})
E_{oc}	open circuit voltage (V)
E^0	open circuit voltage for unit activities of all participating species (V)
$E^{0'}$	formal potential (V)
f	function representing the 1-D explicit model
F	Faraday's constant (96,487 C mole^{-1})
g	function representing the 1-D implicit and 2-D models
i	cell current density (A m^{-2})
i_j^0	exchange current density for electrode j (A m^{-2})
$i_{j,1}$	limiting current density for electrode j (A m^{-2})
i_m	current density calculated using the 1-D implicit and 2-D models (A m^{-2})
$K_{\text{H}_2\text{O}}$	$P_{\text{H}_2\text{S,in}}(2P - P_{\text{H}_2\text{O,in}})/P_{\text{H}_2\text{O,in}}(2P + P_{\text{H}_2\text{S,in}})$
K_{S_2}	$P_{\text{H}_2\text{S,in}}(P - P_{\text{S}_2,\text{in}})/P_{\text{S}_2,\text{in}}(2P + P_{\text{H}_2\text{S,in}})$
l_j	length or thickness of j (m)
m_j	integration constant for voltage profile in phase j
n	number of i–V data points used in parameter estimation routine
n_e	number of electrons transferred
p	gauge pressure, solved for in the flow subdomains in the 2-D models (Pa)
P	total pressure (bar)
P_k	partial pressure of k (bar)
$P_{k,\text{in}}$	inlet partial pressure of k (bar)
r	distance in radial direction (m)
R	gas constant (8.314 J mole^{-1} K^{-1})
R_{contact}	sum of contact and lead ohmic resistances (Ω)
T	temperature (K)
u	radial component of mass average velocity (m s^{-1})
v	axial component of mass average velocity (m s^{-1})
$\tilde{v}$	molar average velocity (m s^{-1})
$\dot{V}$	temperature corrected volumetric flow-rate (m^3 s^{-1})
V_{cell}	cell voltage (V)
V_m	cell voltage calculated using the 1-D explicit model (V)
w_k	mass fraction of component k
x_k	mole fraction of component k
z	distance in axial direction (m)

Vectors and matrices

$\mathbf{I}$	identity matrix
$\mathbf{i}$	current density vector (A m^{-2})
$\mathbf{j}_i$	diffusive mass flux of component i (kg m^{-2} s^{-1})
$\mathbf{n}$	normal vector (m)
$\mathbf{N}_k$	the total mass flux of the k^{th} component (kg m^{-2} s^{-1})
$\mathbf{p}$, $\mathbf{p}^*$	vectors of parameter values needed to solve the model equations
$\mathbf{t}$	tangent vector (m)
$\mathbf{v}$	mass average velocity vector (m s^{-1})

Greek letters

β	charge transfer coefficient in Butler–Volmer equation
ϵ_j	porosity of phase j
η_{act}	activation losses (V)
η_{conc}	concentration losses (V)
κ_j	permeability in electrode j (m^2)
μ	viscosity (kg (ms)$^{-1}$)
φ_j	electrical potential of phase j
ρ	density (kg m^{-3})
σ_j	electrical conductivity of phase j (Ω^{-1} m^{-1})
τ_j	tortuousity of phase j
$\Delta\phi_j^0$	stoichiometric coefficient for component k equilibrium potential for electrode j (V)

There are two possible overall reactions that use H_2S directly in a SOFC:

$$H_2S + \tfrac{1}{2}O_2 \Leftrightarrow H_2O + \tfrac{1}{2}S_2 \quad (1)$$

$$H_2S + \tfrac{3}{2}O_2 \Leftrightarrow H_2O + SO_2 \quad (2)$$

At the operating temperatures of a SOFC, these reactions are equally favoured thermodynamically and thus produce equilibrium voltages that are very close to each other, e.g., 0.782 V for the first and 0.75 V for the second at 800 °C [8]. Besides these reactions, part of the H_2S fed dissociates into H_2 and S_2 and the H_2 can then undergo electrochemical oxidation.

It is not yet fully clear which (if any) of these reactions predominates in a SOFC running on H_2S. Some of the above mentioned studies have attempted to figure out which of the above electrochemical reactions predominates on the anode by looking at the open circuit voltage (OCV) [8] and analyzing the anode exhaust gases [4]. However, the only broadly accepted conclusion drawn has been that a H_2S SOFC produces more SO_2 at higher loads and more S_2 closer to OCV [7].

1.1. Modelling SOFCs

Mathematical models of fuel cells are design and optimization tools that can help in selecting operating conditions, cell materials, stack design, controller design, among other things. The above capabilities depend on the ability to quickly modify operating conditions or revamp cell design in the model and

examine the effects on cell or stack performance. Thus, models enable simulations or numerical experiments that can dramatically decrease development time for a fuel cell design [15].

As with any fuel cell system, SOFCs can be modelled on many levels. Models have been built at the electrode, single cell, and cell stack levels. The earliest studies by Debendetti and Vayenas [16] were on the single cell level. This model was later extended to model a layer of cells in a cross-flow stack [17]. These models were 2-D in nature and only modelled the average concentrations and temperature in each cell in the stack layer, while ignoring mass transfer and electrochemical kinetics. Since these studies, a large number of models with varying levels of complexity and detail have been built, and a good review can be found in ref. [18].

In this work we are modelling the fuel cell investigated by Liu et al. [6]. The electrodes and electrolyte assembly is in the shape of a circular disc held between the air outlet tube on one side and the fuel outlet tube on the other. On both sides, inflow occurs through the inner one and the outflow through the outer tube. Both the air and fuel sides are at atmospheric pressure. This geometry is very common and is also known as a "button cell". The data sets that are used in this work to validate the models are from a sample cell that used Co–Mo–S mixed with Ag as anode, and Pt as cathode. The electrolyte was 8 mole% YSZ. The cell assembly and the gas feeds and outlets are held in a temperature controlled furnace.

In this paper we present four different models of increasing complexity and examine their fit to experimental data given in Ref. [6]. Of these, the first two are one-dimensional models that solve for the electrochemistry as well as electrical potential and mass transfer in the electrodes. We start with the simplest model possible that explicitly calculates the output voltage of the cell given the current being drawn from it. This model is derived using a one-dimensional analysis along the axis of the cell and calculates the three voltage loss terms: the electrical resistance losses, the mass transfer losses, and the electrochemical activation losses separately by ignoring the coupling between the mass transfer and electrochemistry. The second model is a refined version of the first where the mass transfer losses and the electrochemical activation losses are coupled and cannot be calculated explicitly. For this model, the performance of the cell is calculated by solving a set of coupled non-linear algebraic equations. The third and fourth models are two-dimensional axi-symmetric models where the flow, mass transfer, voltage fields, and electrochemical reaction are all modelled. The fourth model is identical to the third, except the diffusive mass transfer is modelled using the multi-component Maxwell–Stefan formulation instead of Fick's law. The resulting coupled partial differential equations are solved using finite element methods (FEM).

In order to solve these models, various parameters such as diffusion coefficients, viscosities, electrical conductivities of the electrodes and electrolyte, and electrochemical reaction rate parameters need to be defined. While many of these parameters are known or can be estimated, some, such as exchange current densities for the electrochemical reactions in the electrodes are not known with any certainty. There are no data on electrochemical kinetic parameters for H_2S anodes in literature. While there are some kinetic data for O_2 reduction on Pt cathodes, there is little agreement in the SOFC research community on the reaction mechanisms [19]. Since there is no reliable data for the electrochemical kinetic parameters, we use non-linear least squares estimation in this work to estimate the kinetic parameters in all four models.

In the body of this paper, we start with a detailed development of all the models used and discuss the model parameters needed. We then introduce the mathematical formulation used for estimating the unknown parameters. The results of the parameter estimation are presented next, and we examine these estimates and the quality of the fit of the models to the experimental data to draw conclusions on the fidelity and usefulness of the models. We end with some thoughts on how these models can be improved and plans for future work.

2. Modelling

The 1-D and 2-D model geometries are given in Fig. 1. In developing the 2-D models, the cylindrical geometry of the experimental cell and the symmetry around the central axis is used to reduce the modelling domain to a 2-D axi-symmetric domain as shown in the top section of Fig. 1. The sub-domains in this reduced domain are (going left to right): (i) the fuel flow channel, $\Omega_{f,\text{fuel}}$ (ii) the anode, Ω_a (iii) the electrolyte, Ω_m (iv) the cathode, Ω_c and (v) the air flow channel, $\Omega_{f,\text{air}}$. The 1-D model geometry, given in the bottom section of Fig. 1 does not consider the flow channels as the inherently 2-D flow field cannot be modelled correctly in a 1-D model.

In the 2-D models, the current collectors are located at the vertical interface between the flow and electrode sub-domains on both sides. In the 1-D model, the anode current collector is the left-most point of the domain while the cathode current collector is the right-most point in the domain.

The main assumptions used in the models presented are:

(1) All models presented are isothermal.
(2) The only electrochemical reaction modelled on the anode is the oxidation of H_2S to H_2O and S_2 (reaction (14)) even though there are probably other reactions occuring simultaneously.
(3) The open circuit voltage is taken as the zero current voltage in the data set being modelled.
(4) In the 1-D models, the absolute pressure is assumed constant in the electrodes.

We explain these assumptions in more detail in relevant subsections.

The assumption that all models are isothermal is justified in the current study for the following reasons:

(1) The experimental cell modelled is in a temperature controlled electric furnace.
(2) The current density drawn from the cell is relatively small, which means the heat generation is also small.
(3) Although the fuel and air streams are not preheated before they are fed to the SOFC, the flow-rates are quite small

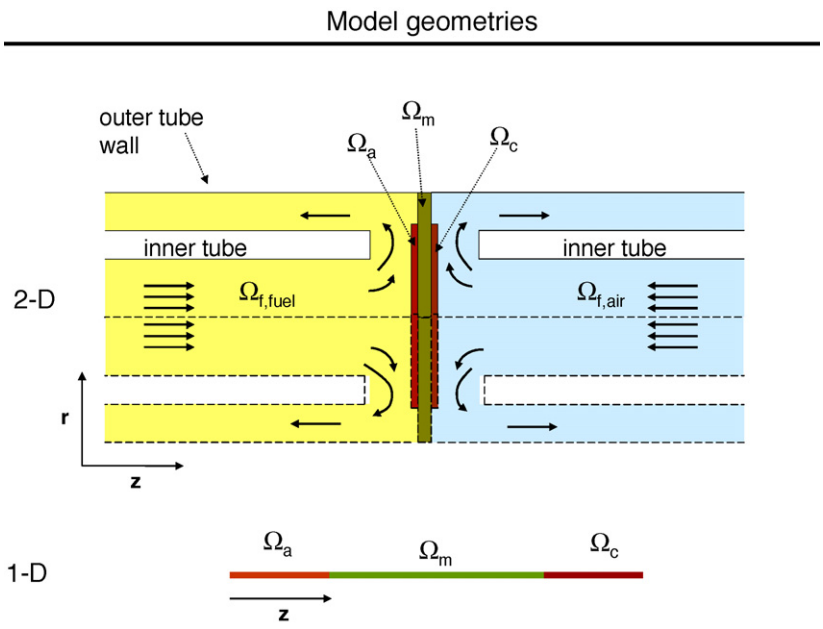

Fig. 1. 1-D and 2-D model geometries (not to scale).

(25 ml min^{-1}) and allow the gases to come up to cell temperature by the time they get to the actual cell. The above was verified by modelling only the fluid flow and heat transfer using the 2-D geometry.

In this work, the one-dimensional models are solved using MATLAB [20] while COMSOL Multiphysics [21] is used to solve the two-dimensional models. MATLAB is a general purpose computational software platform and language. COMSOL Multiphysics is a finite element method based modelling package for the simulation of any physical process that can be described using ordinary or partial differential equations. It has an easy to use graphic user interface that handles all modelling steps from geometry generation and meshing, to defining the differential equations and boundary conditions, to solving and post-processing the results. COMSOL Multiphysics has a MATLAB interface that allows easy transfer of data from one to the other. It is this interface that allows the use of optimization routines available in MATLAB for the parameter estimation described later.

2.1. Open circuit voltage

In most fuel cell models, the open circuit voltage or the equilibrium voltage across a fuel cell is calculated using the Nernst equation [22]. In all the models discussed in this work, however, the open circuit voltage, E_{oc} is taken from experimental data instead of being calculated using the Nernst equation. This is done for the following reasons:

- The open circuit voltage in a H_2S SOFC is probably a mixed voltage from the different possible reactions at the anode [4,7,8]. Modelling a mixed voltage requires that the kinetics of each possible electrochemical reaction be considered. This in turn requires additional kinetic parameter values for each reaction, and as discussed earlier, these are unavailable for the anode used in the experiments. This is also the reason why reaction (1) is the only electrochemical reaction modelled in this study.
- Nernst equation requires the compositions of the products (H_2O and S_2 for reaction (1)) as well as the reactants. These were not measured during the experiments that are being modelled in this study.

2.2. 1-D explicit model

In developing this model we followed a similar approach to that detailed in Kim et al. [23] and Chan et al. [24]. A one-dimensional analysis was done along the thickness of the cell (Fig. 1) to obtain a model Eq. (3) that relates the voltage of the working cell, V_{cell} to the current density, i drawn from the cell:

$$V_{cell} = E_{oc} - iR_{\Omega} - \eta_{act,anode} - \eta_{act-cathode} - \eta_{conc,anode} - \eta_{conc-cathode} \quad (3)$$

where R_{Ω} is the total ohmic resistance (cell area specific) of the cell, η_{act} the activation voltage losses at the anode and cathode, and η_{conc} are the concentration (mass transfer) voltage losses. The activation and concentration (mass transfer) voltage losses in our model are given in Eqs. (4)–(8) below:

$$R_{\Omega} = \left.\frac{l}{\sigma}\right|_{YSZ} + \left.\frac{l}{\sigma}\right|_{anode} + \left.\frac{l}{\sigma}\right|_{cathode} + R_{contact} \quad (4)$$

$$\eta_{act,anode} = \frac{2RT}{n_e F} \sin h^{-1}\left(\frac{i}{2i_a^0}\right) \quad (5)$$

$$\eta_{act-cathode} = \frac{2RT}{n_e F} \sin h^{-1}\left(\frac{i}{2i_c^0}\right) \quad (6)$$

$$\eta_{\text{conc,anode}} = -\frac{RT}{2F}\ln\left(\frac{1 - i/i_{a,1}}{(1 + K_{H_2O}\, i/i_{a,1})\sqrt{1 + K_{S_2}\, i/i_{a,1}}}\right) \tag{7}$$

$$\eta_{\text{conc-cathode}} = -\frac{RT}{4F}\ln\left(1 - \frac{i}{i_{c,1}}\right) \tag{8}$$

$$i_{a,1} = \frac{P_{H_2S,\text{in}}}{(2 + P_{H_2S,\text{in}}/P)}\frac{4FD_{H_2S,\text{eff}}}{RTl_a} \tag{9}$$

$$i_{c,1} = \frac{P_{O_2,\text{in}}}{(1 - P_{O_2,\text{in}}/P)}\frac{4FD_{O_2,\text{eff}}}{RTl_c} \tag{10}$$

where l is the length, σ the electrical conductivity of the electrode or electrolyte, n_e the number of electrons transferred in the electrode reaction, and P is the total or absolute pressure. For both the 1-D models, we assume that P is constant at 1.013×10^5 Pa in both electrodes. The ohmic resistance, given by Eq. (4), includes the area specific resistance of the zirconia electrolyte, the electrodes and the contact resistance. Any current lead wire or inter-phase resistance is bundled into R_{contact}. The activation losses assume a Butler–Volmer [22] kinetic expression where the charge transfer coefficients are 0.5, and i_a^0, i_c^0 are the exchange current densities. K_{H_2O} in Eq. (7) is a function of initial partial pressures of H_2O and H_2S, while K_{S_2} is a function of initial partial pressures of S_2 and H_2S. The concentration voltage loss terms have the limiting current densities $i_{a,1}$ and $i_{c,1}$ as parameters, which in turn are functions of, among other things, the effective diffusivities of the reactants, $D_{k,\text{eff}}$. Effective diffusivity is a function of the bulk diffusivity D_k, Knudsen diffusivity $D_{K,k}$, and the ratio of porosity to tortuousity ϵ/τ:

$$D_{k,\text{eff}} = \frac{\epsilon/\tau}{D_k^{-1} + D_{K,k}^{-1}} \tag{11}$$

The solutions to the mass transfer equations for the reactants and products are used to obtain the above terms for the concentration losses. The form of the mass transfer equations, and thus the solutions are identical to those for the 1-D implicit model discussed in the next section. These solutions or concentration profiles Eqs. ((24)–(26)), however, need to be linearized in order to get the explicit form for the concentration losses. Of course, the 1-D explicit model does not consider the coupling between the activation and concentration losses as the form of the Butler–Volmer equation used Eqs. (5) and (6) does not contain any concentration terms, while the 1-D implicit model does so through the concentration terms in the electrochemical rate equations Eqs. (20) and (21).

2.3. 1-D implicit model

The governing ordinary differential equations (ODEs) used in our 1-D implicit model are presented in this section. A 1-D model for this geometry cannot consider flow and mass transfer in the channels. Thus, the model equations only need to describe the mass transfer in the electrodes and the voltage distribution in the anode, cathode, and electrolyte. The model domain is a line that extends from the current collector on the anode to the current collector on the cathode along the axis of the cell and includes the electrodes and the electrolyte (see bottom of Fig. 1).

2.3.1. Governing equations: mass transfer and voltage

2.3.1.1. Mass transfer. The reactants, oxygen on the cathode side and hydrogen sulfide on the anode side, are transported from the flow channels to their respective electrode–electrolyte interfaces where the reaction occurs. Similarly, the products on the anode side are transported from the anode–electrolyte interface into the fuel flow channel. This mass transfer of the reactants and products is modelled using the convection–diffusion equation:

$$\frac{\mathrm{d}}{\mathrm{d}z}\left\{-D_{k,\text{eff}}\frac{\mathrm{d}C_k}{\mathrm{d}z} + \tilde{v}C_k\right\} = 0 \tag{12}$$

$$\tilde{v} = -\frac{i}{FC_t}\sum_k \frac{\xi_k}{n_k} \tag{13}$$

where C_k is the molar concentration of the k^{th} component, C_t the total molar concentration, and $\tilde{v}$ is the mole average velocity of the gas. $k = \{H_2S, H_2O, S_2\}$ in the anode and $\{O_2\}$ in the cathode. As no carrier gas is used on the anode side in the experiments, we can model transport of H_2S and H_2O on the anode side and obtain the concentration of S_2 at any point by using the identity: $C_{S_2} = C_t - C_{H_2S} - C_{H_2O}$. We obtain Eq. (13) for $\tilde{v}$ by considering the overall molar flux towards or away from the reaction interface and assuming that the total pressure, and thus the concentration remains constant in the electrodes.

2.3.1.2. Potential distribution. The fuel reacts on the anode–electrolyte interface and releases electrons. These electrons travel through the anode to the outer circuit and come around through the cathode to the cathode–electrolyte interface where they are consumed in the reaction with oxygen. To complete the circuit, the oxide ions produced at the cathode–electrolyte interface travel across the electrolyte to the anode–electrolyte interface:

$$H_2S + O^{2-} \Leftrightarrow H_2O + \tfrac{1}{2}S_2 + 2e^- \tag{14}$$

$$O_2 + 4e^- \Leftrightarrow 2O^{2-} \tag{15}$$

The voltage and current distribution in the electrodes and the electrolyte due to this electronic and ionic transport is modelled using Ohm's law:

$$\frac{\mathrm{d}}{\mathrm{d}z}\left(-\sigma_j\frac{\mathrm{d}\phi_j}{\mathrm{d}z}\right) = 0 \tag{16}$$

where σ_j is the electrical conductivity and ϕ_j is the electrical potential of the j^{th} sub-domain (anode, electrolyte, or cathode).

2.3.2. Boundary conditions

To get the concentration and voltage profiles, the following boundary conditions need to be solved:

- Concentrations of O_2 in air, and H_2S, H_2O in fuel given at the inlets:

$$\begin{aligned} C_{H_2S}|_{\partial\Omega_{fuel,inlet}} &= C_{H_2S,in} \\ C_{H_2O}|_{\partial\Omega_{fuel,inlet}} &= C_{H_2O,in} \\ C_{O_2}|_{\partial\Omega_{air,inlet}} &= C_{O_2,in} \end{aligned} \tag{17}$$

- Molar flux, of the reactants into, and the products out of, the electrolyte governed by the local current density at the electrode–electrolyte interface:

$$\begin{aligned} \left(-D_{H_2S,eff}\frac{dC_{H_2S}}{dz} - \frac{i_{anode}C_{H_2S}}{4FC_t}\right)\Big|_{\partial\Omega_{anode,electrolyte}} &= \frac{i_{anode}}{2F} \\ \left(-D_{H_2O,eff}\frac{dC_{H_2O}}{dz} - \frac{i_{anode}C_{H_2S}}{4FC_t}\right)\Big|_{\partial\Omega_{anode,electrolyte}} &= -\frac{i_{anode}}{2F} \\ \left(-D_{O_2,eff}\frac{dC_{O_2}}{dz} - \frac{i_{cathode}C_{O_2}}{4FC_t}\right)\Big|_{\partial\Omega_{cathode,electrolyte}} &= -\frac{i_{cathode}}{4F} \end{aligned} \tag{18}$$

- The voltage at the anode and cathode current collectors is specified:

$$\begin{aligned} -\sigma_a\frac{d\phi_a}{dz}\Big|_{\partial\Omega_{anode,collector}} &= (\phi_a - 0)\left[\frac{\sigma}{l}\right]_{contact} \\ -\sigma_c\frac{d\phi_c}{dz}\Big|_{\partial\Omega_{cathode,collector}} &= (\phi_c - V_{cell})\left[\frac{\sigma}{l}\right]_{contact} \end{aligned} \tag{19}$$

where $[\sigma/l]_{contact}$ is the reciprocal of the area specific contact and lead resistance for each electrode.

- Current density at the electrode–electrolyte interfaces is given by the electrochemical reaction rate, which is dependent on the local concentrations of the active species and the local voltage difference between the electrode and the electrolyte [22]:

$$-\sigma_a\frac{d\phi_a}{dz}\Big|_{\partial\Omega_{anode,electrolyte}} = i_a^0\left\{\frac{C_{H_2S}}{C_{H_2S,ref}}\exp\left(\frac{2(1-\beta)\eta_a F}{RT}\right) - \frac{C_{H_2O}}{C_{H_2O,ref}}\sqrt{\frac{C_{S_2}}{C_{S_2,ref}}}\exp\left(\frac{-2\beta\eta_a F}{RT}\right)\right\} \tag{20}$$

$$-\sigma_c\frac{d\phi_c}{dz}\Big|_{\partial\Omega_{cathode,electrolyte}} = i_c^0\left\{\sqrt{\frac{C_{O_2}}{C_{O_2,ref}}}\exp\left(\frac{-2\beta\eta_c F}{RT}\right) - \exp\left(\frac{2(1-\beta)\eta_c F}{RT}\right)\right\} \tag{21}$$

$$\begin{aligned} -\sigma_a\frac{d\phi_a}{dz}\Big|_{\partial\Omega_{anode,electrolyte}} &= -\sigma_m\frac{d\phi_m}{dz}\Big|_{\partial\Omega_{anode,electrolyte}} \\ -\sigma_c\frac{d\phi_c}{dz}\Big|_{\partial\Omega_{cathode,electrolyte}} &= -\sigma_m\frac{d\phi_m}{dz}\Big|_{\partial\Omega_{cathode,electrolyte}} \end{aligned} \tag{22}$$

$$\begin{aligned} \eta_a &= \phi_{anode} - \phi_{electrolyte} - \Delta\phi_a^0; \\ \eta_c &= \phi_{cathode} - \phi_{electrolyte} - \Delta\phi_c^0 \end{aligned} \tag{23}$$

where i_a^0 and i_c^0 are the exchange current densities of the anode and cathode, β the charge transfer coefficient, $C_{k,ref}$ the reference (in this case, inlet) component densities and $\Delta\phi_a^0$ and $\Delta\phi_c^0$ are the anode and cathode equilibrium potentials.

The boundary conditions given by Eqs. (20) and (21) are called electrochemical rate equations because while a chemical rate equation depends on local species concentrations, an electrochemical rate equation depends on local species concentrations as well as the local potential difference between the electrode and electrolyte phases.

Solution of the mass transfer ODEs and boundary conditions gives the component partial densities and electric potentials as functions of current density and distance from the anode current collector along the cell axis:

$$C_{H_2S} = -2C_t + (2C_t + C_{H_2S,in})\exp\left(-\frac{iz}{4C_tFD_{H_2S,eff}}\right) \tag{24}$$

$$C_{H_2O} = 2C_t + (-2C_t + C_{H_2O,in})\exp\left(-\frac{iz}{4C_tFD_{H_2O,eff}}\right) \tag{25}$$

$$C_{O_2} = C_t + (-C_t + C_{O_2,in})\exp\left(-\frac{i[z-(l_a+l_m+l_c)]}{4C_tFD_{O_2,eff}}\right) \tag{26}$$

$$\phi_j = m_j z + c_j \tag{27}$$

where m_j and c_j are integration constants for the voltage profile equation for the j^{th} sub-domain (anode, electrolyte, or cathode).

Although we obtain the concentration profiles above, they are functions of the current density which in turn is a function of the concentrations at the inter phase boundaries. The electric potential boundary conditions Eqs. ((19)–(23)) provide a set of coupled non-linear algebraic equations that cannot be solved analytically. In this work, these six equations in six unknowns (m_j and c_j), are solved numerically using MATLAB [20].

2.4. 2-D models

The first 2-D model, built using COMSOL Multiphysics [21], solves the (i) non-isothermal flow equations and Darcy's law for velocity and pressure in the flow channels and electrodes, respectively, (ii) convection–diffusion mass transfer equations for partial densities of H_2S, H_2O, S_2 on the fuel side and O_2 on the air side and, (iii) Laplace equation (Ohm's law) for the voltage/current distribution in the electrodes and electrolyte.

The second 2-D model uses the Maxwell–Stefan equations (instead of Fick's law) to model the multicomponent mass transfer in the fuel cell.

2.4.1. Flow in gas channels

The fluid flow in the fuel and air channels is important as it describes the transport of reactants to and the products from the cell. The non-isothermal flow mode is used here because the composition changes in the fuel and air channels lead to small density variations. These density variations are taken into account by adding a term to the momentum equations and modifying the continuity equation as shown in the governing PDEs for the flow fields:

$$-\nabla\cdot\left[\mu(\nabla\mathbf{v}+(\nabla\mathbf{v})^{\mathrm{T}})-\tfrac{2}{3}\mu(\nabla\cdot\mathbf{v})\mathbf{I}\right]+\rho(\mathbf{v}\cdot\nabla\mathbf{v})+\nabla p=0,\quad \nabla\cdot(\rho\mathbf{v})=0 \tag{28}$$

where μ is the viscosity of the fluid, $\mathbf{v}$ the velocity vector, ρ the density, p the pressure, and $\mathbf{I}$ is the identity matrix.

2.4.1.1. Boundary conditions (channel flow).

- Zero velocity (no-slip) at the walls:

$$\mathbf{v}=0|_{\partial\Omega_{\mathrm{walls}}} \tag{29}$$

- Velocity continuous across the channel–electrode interfaces:

$$\mathbf{v}^{\text{flow channels}}=\mathbf{v}^{\text{electrodes}}\Big|_{\partial\Omega_{\text{flow channels}-\text{electrodes}}} \tag{30}$$

- Fully developed laminar flow at the fuel and air inlets. Given the volumetric flow-rate, the axial velocity profile is calculated as:

$$u=0,\quad v=\frac{2\dot{V}}{\pi r_i^2}\left[1-\left(\frac{r}{r_i}\right)^2\right] \tag{31}$$

where u and v are the r and z components of the velocity vector, $\dot{V}$ the temperature corrected volumetric flow-rate, and r_i is the inner radius for the inlet tube.

- Pressure specified and flow normal to the boundary at the outlets of the flow channels:

$$p=0,\quad \mathbf{t}\cdot\mathbf{v}=0 \tag{32}$$

where $\mathbf{t}$ is the tangential vector.

- Radial symmetry along the axis of the flow channels:

$$\left.\frac{\partial v}{\partial r}\right|_{r=0}=0,\quad u|_{r=0}=0 \tag{33}$$

2.4.2. Flow in electrodes

The flow in the porous electrodes is modelled using Darcy's law:

$$\mathbf{v}=-\frac{\kappa}{\mu}\nabla p,\quad \nabla\cdot(\rho\mathbf{v})=0 \tag{34}$$

where κ is the permeability of the porous electrode.

2.4.2.1. Boundary conditions (electrode flow).

- Pressure at each electrode-flow channel interface is equal to the pressure in the flow channel at that interface:

$$p_{\text{anode}}|_{\partial\Omega_{\text{anode,fuel channel}}}=p_{\text{fuel channel}}|_{\partial\Omega_{\text{anode,fuel channel}}} \tag{35}$$

$$p_{\text{cathode}}|_{\partial\Omega_{\text{cathode,air channel}}}=p_{\text{air channel}}|_{\partial\Omega_{\text{cathode,air channel}}} \tag{36}$$

- Flow into the electrodes at the electrode–electrolyte interface is the net difference in the amount of the products being formed and the reactants being consumed at that interface:

$$-\mathbf{n}.\mathbf{v}|_{\partial\Omega_{\text{electrode,electrolyte}}}=\frac{1}{\rho}\left(\frac{i_{\text{electrode}}}{F}\sum_k\frac{\xi_k M_K}{n_k}+\sum_k\mathbf{n}\cdot\mathbf{j}_k\right) \tag{37}$$

where $\mathbf{n}$ is the normal vector, $i_{\text{electrode}}$ the current density, F the Faraday's constant, ξ_k the stoichiometric coefficient, M_k the molar weight, n_k the number of electrons transferred per molecule, and $\mathbf{j}_k$ is the diffusive flux of the k^{th} component.

- Radial symmetry along the axis of the cell:

$$\left.\frac{\partial p}{\partial r}\right|_{r=0}=0 \tag{38}$$

2.4.3. Mass transfer

Two mass transfer models are used for the 2-D fuel cell models in this work. The convection–diffusion Eq. (39) is used in both models to descibe the mass transfer of the reactants and products in the flow channels and the electrodes:

$$\nabla\cdot\mathbf{j}_i+\rho\mathbf{v}\cdot\nabla w_i=0 \tag{39}$$

The diffusive flux is given by Fick's law Eq. (40) in the first 2-D model, and by the Maxwell–Stefan diffusive flux Eq. (41) in the second [25]:

$$\mathbf{j}_i=-\rho\bar{D}_i\nabla(w_i) \tag{40}$$

where $\mathbf{j}_i$ is the diffusive flux of i, ρ the density of the gas mixture and w_i is the mass fraction of the i^{th} component. $\bar{D}_i$ is the diffusivity of component i: bulk diffusivity in the flow channels, effective diffusivity in the electrodes. Mass fractions are used instead of mole fractions or molar concentrations in the Fick diffusive flux term because the mass transfer is coupled to the fluid flow equations where the fluid velocity $\mathbf{v}$ is a mass average quantity:

$$\mathbf{j}_i=-\rho w_i\sum_{j=1}^{n}\tilde{D}_{ij}\left(\nabla x_j+(x_j-w_j)\frac{\nabla p}{p}\right) \tag{41}$$

In Eq. (41), n is the total number of species in the mixture, x_j is the mole fraction of species j, and $\tilde{D}_{ij}$ is the multicomponent composition dependent diffusivity of species i in j, which is given by:

$$\frac{x_i x_k}{D_{ik}}=-w_i w_k\frac{\sum_{j\neq i}(\text{adj }B_i)_{jk}}{\sum_{j\neq i}\tilde{D}_{ij}(\text{adj }B_i)_{jk}},\quad (B_i)_{kj}=D_{kj}-D_{ij},\quad i\neq j \tag{42}$$

where D_{ik} are multicomponent Maxwell–Stefan diffusivities that for low density gas mixtures can be approximated by composition independent binary diffusivities, and can be estimated using the Fuller, Schettler and Giddings equation. The values used in this work are given in Section 2.5.

Mass fractions and mole fractions are related through:

$$w_j = \frac{x_j M_j}{\sum_j x_j M_j} \tag{43}$$

For Fick's law, effective diffusivity in the electrodes is defined in Eq. (11), but for Maxwell–Stefan mass transfer, Eq. (44) is used:

$$D_{ik,\text{eff}} = \frac{\epsilon}{\tau} D_{ik} \tag{44}$$

As discussed earlier, no carrier gas is used on the anode side in the experiments. Thus, we can model transport of H_2S and H_2O on the anode side and obtain the mass fraction of S_2 at any point by using the identity: $w_{s_2} = 1 - w_{H_2S} - w_{H_2O}$

2.4.3.1. Boundary conditions (convection–diffusion equation).

- Mass fraction of O_2 in air, and H_2S, S_2, H_2O in fuel given at the flow channel inlets:

$$\begin{aligned} w_{H_2S}|_{\partial\Omega_{\text{fuel,inlet}}} &= w_{H_2S,\text{in}} \\ w_{H_2O}|_{\partial\Omega_{\text{fuel,inlet}}} &= w_{H_2O,\text{in}} \\ w_{O_2}|_{\partial\Omega_{\text{air,inlet}}} &= w_{O_2,\text{in}} \end{aligned} \tag{45}$$

- Zero flux at the inner and outer tube walls:

$$\begin{aligned} \mathbf{n}\cdot\mathbf{N}_k|_{\partial\Omega_{\text{walls}}} &= 0 \\ \mathbf{N}_k &= \mathbf{j}_k + \rho w_k \mathbf{v} \end{aligned} \tag{46}$$

where $\mathbf{N}_k$ is the total mass flux of the k^{th} component.

- Mass flux, of the reactants out of, and the products into, the electrodes governed by the local current density at the electrode–electrolyte interface:

$$\begin{aligned} -\mathbf{n}\cdot\mathbf{N}_{H_2S}|_{\partial\Omega_{\text{anode,electrolyte}}} &= -\frac{M_{H_2S} i_{\text{anode}}}{2F} \\ -\mathbf{n}\cdot\mathbf{N}_{H_2O}|_{\partial\Omega_{\text{anode,electrolyte}}} &= \frac{M_{H_2O} i_{\text{anode}}}{2F} \\ -\mathbf{n}\cdot\mathbf{N}_{O_2}|_{\partial\Omega_{\text{cathode,electrolyte}}} &= -\frac{M_{O_2} i_{\text{cathode}}}{4F} \end{aligned} \tag{47}$$

- Radial symmetry along the axis of the flow channels and the electrodes:

$$\left.\frac{\partial w_k}{\partial r}\right|_{r=0} = 0 \tag{48}$$

2.4.4. Voltage and current distribution

The voltage and current distribution in the electrodes and the electrolyte due to this electronic and ionic transport is modelled using the vector form of Ohm's law:

$$\begin{aligned} \nabla\cdot(-\sigma_m\nabla\phi_m) &= 0 \\ \nabla\cdot(-\sigma_a\nabla\phi_a) &= 0 \\ \nabla\cdot(-\sigma_c\nabla\phi_c) &= 0 \end{aligned} \tag{49}$$

where σ_m, σ_a, σ_c are electrical conductivities of the electrolyte, anode and cathode, and ϕ_m, ϕ_a, ϕ_c are electrical potentials of the electrolyte, anode, and cathode.

2.4.4.1. Boundary conditions (Ohm's law).

- The voltage at the anode and cathode current collectors is specified:

$$\begin{aligned} \mathbf{n}\cdot\mathbf{i}_{\text{anode}}|_{\partial\Omega_{\text{anode,collector}}} &= (\phi_a - 0)\left[\frac{\sigma}{l}\right]_{\text{contact}} \\ \mathbf{n}\cdot\mathbf{i}_{\text{cathode}}|_{\partial\Omega_{\text{cathode,collector}}} &= (\phi_c - V_{\text{cell}})\left[\frac{\sigma}{l}\right]_{\text{contact}} \\ \mathbf{i}_j &= -\sigma_j\nabla\phi_j \end{aligned} \tag{50}$$

where $\mathbf{i}$ is the current density vector $[\sigma/l]_{\text{contact}}$ is the area specific contact and lead conductance.

- Electrical insulation at the outer tube walls:

$$\begin{aligned} \mathbf{n}\cdot\mathbf{i}_{\text{anode}}|_{\partial\Omega_{\text{walls}}} &= 0 \\ \mathbf{n}\cdot\mathbf{i}_{\text{cathode}}|_{\partial\Omega_{\text{walls}}} &= 0 \\ \mathbf{n}\cdot\mathbf{i}_{\text{electrolyte}}|_{\partial\Omega_{\text{walls}}} &= 0 \end{aligned} \tag{51}$$

- Current density at the electrode–electrolyte interfaces is given by the electrochemical reaction rate, which is dependent on the local concentrations of the active species and the local voltage difference between the electrode and the electrolyte:

$$-\mathbf{n}\cdot\mathbf{i}_{\text{anode}}|_{\partial\Omega_{\text{anode,electrolyte}}} = i_a^0\left\{\frac{x_{H_2S}}{x_{H_2S,\text{ref}}}\exp\left(\frac{2(1-\beta)\eta_a F}{RT}\right) - \frac{x_{H_2O}}{x_{H_2O,\text{ref}}}\sqrt{\frac{x_{S2}}{x_{S_2,\text{ref}}}}\exp\left(\frac{-2\beta\eta_a F}{RT}\right)\right\} \tag{52}$$

$$-\mathbf{n}\cdot\mathbf{i}_{\text{cathode}}|_{\partial\Omega_{\text{cathode,electrolyte}}} = i_c^0\left\{\sqrt{\frac{x_{O_2}}{x_{O_2,\text{ref}}}}\exp\left(\frac{-2\beta\eta_c F}{RT}\right) - \exp\left(\frac{2(1-\beta)\eta_c F}{RT}\right)\right\} \tag{53}$$

$$\begin{aligned} \eta_a &= \phi_{\text{anode}} - \phi_{\text{electrolyte}} - \Delta\phi_a^0; \\ \eta_c &= \phi_{\text{cathode}} - \phi_{\text{electrolyte}} - \Delta\phi_c^0 \end{aligned} \tag{54}$$

where i_a^0 and i_c^0 are the exchange current densities of the anode and cathode, β the charge transfer coefficient, x_k the mole fractions at the boundary, $x_{k,\text{ref}}$ the reference (in this case, inlet) mole fractions and $\Delta\phi_a^0$ and $\Delta\phi_c^0$ are the anode and cathode equilibrium potentials.

- Radial symmetry along the axis of the electrodes and the electrolyte:

$$\left.\frac{\partial\phi_j}{\partial r}\right|_{r=0} = 0 \tag{55}$$

The mesh generated for the 2-D models above had 3853 triangular elements, which translates to 30,229 degrees of freedom.

We used the non-linear parametric solver (with the UMFPACK direct solver for the linear subsystem) in COMSOL Multiphysics to solve the model at equally spaced voltage intervals from near OCV to 0 V. Grid independence of the results was insured by comparing the model output for the current density at 0 V and 850 °C, against a mesh 4 times denser. The relative error in the calculated current denstiy was of the order of 10^{-6} between the mesh used in this work (with 3853 elements) and the test mesh with 15,412 elements.

2.5. Parameters used in the models

There are a number of parameters in the models presented above and these parameters need to be estimated before the models can be solved. Physical constants, such as the gas constant R, and the values assigned to them in the models are summarized in Nomenclature. Transport parameters needed include diffusivities, viscosities, and electrical conductivities, while the electrochemical parameters needed are equilibrium electrode potential, exchange current density and the charge transfer coefficient for each electrode.

Binary diffusion coefficients D_{ij} are estimated using the Fuller, Schettler and Giddings relation given in Reid et al. [26]. Knudsen diffusion coefficients $D_{K,k}$ are calculated assuming smooth round pores. Viscosity of the gases on both sides of the fuel cell μ_{air},μ_{fuel} is also estimated using Brokaw's method outlined in Ref. [26]. The densities of the gases are calculated using the ideal gas law and the mass fractions of the components. Experimental values for electrode permeability κ were not available and order of magnitude estimates are used based on permeability values calculated for close packings of spheres [27].

Electrical conductivity of the anode materials σ_a used was measured by Liu [28] and those values are used in this work. The cathode used in the experiments was Pt, and the value for Pt conductivity at the operating temperatures is corrected for porosity using relations given in Ref. [29]. Values for conductivity of the YSZ electrolyte σ_m are obtained using the temperature dependent form given in Ref. [30].

The equilibrium potential of the cathode $\Delta\phi_c^0$ is set to the value of the open circuit potential at each operating temperature while the equilibrium potential of the anode $\Delta\phi_a^0$ is set to zero. The open circuit potential at each operating temperature is taken from the experimental i–V data sets. The charge transfer symmetry coefficients β in the electrochemical rate equations Eqs. (20), (21), (52) and (53) are assigned the default value of 0.5 [22]. As experimental values for exchange current densities are not available, we estimate them using our models and experimental i–V data. The estimation procedure is explained in the next section.

The overall wire lead and contact resistance is calculated by comparing the cell's i–V curve to the IR compensated i–V curve at the different operating temperatures. The overall cell area specific resistance is given by Eq. (56), where V_{IR} is the IR compensated cell voltage and V is the actual cell voltage when a current density of i is drawn from the cell. Four such values taken at different points of the i–V curve are averaged and the known resistances of the different cell layers are subtracted from the overall resistance to obtain the overall wire lead and contact resistance for the cell Eq. (57). This overall resistance is then divided into equal halves in our models and placed at the current collectors for each electrode:

$$R_\Omega = \frac{V_{IR} - V}{i} \tag{56}$$

$$\left[\frac{l}{\sigma}\right]_{\text{contact},t} = R_\Omega - \left[\frac{l}{\sigma}\right]_{\text{YSZ}} - \left[\frac{l}{\sigma}\right]_{\text{anode}} - \left[\frac{l}{\sigma}\right]_{\text{cathode}} \tag{57}$$

$$\left[\frac{l}{\sigma}\right]_{\text{contact}} = \frac{1}{2}\left[\frac{l}{\sigma}\right]_{\text{contact},t} \tag{58}$$

The numerical values of all the parameters used are given in Tables 1 and 2.

Table 1
Temperature independent parameters in the models

Parameter	Value
P (Pa)	1.013×10^5
$\dot{V}_{fuel}$ (ml min^{-1})	25
$\dot{V}_{air}$ (ml min^{-1})	25
$x_{H_2S,in}$	0.985
$x_{H_2O,in}$	0.01
$x_{O_2,in}$	0.21
ϵ	0.4
τ	4
$r_{pore,av}$ (m)	2×10^{-6}
l_a (m)	10^{-4}
l_c (m)	10^{-4}
l_m (m)	2×10^{-4}
κ_a (m^2)	10^{-14}
κ_c (m^2)	10^{-14}

3. Parameter estimation

As discussed earlier, the electrochemical parameters on the anode side are completely unknown whereas those on the cathode side are uncertain. In this work we estimate exchange current densities i_a^0 and i_c^0 using non-linear least squares [31]. This

Table 2
Temperature dependent parameter values used

Parameter	750 °C	800 °C	850 °C
D_{H_2S,H_2O} (m^2)	1.89×10^{-4}	2.05×10^{-4}	2.23×10^{-4}
D_{H_2S,S_2} (m^2)	9.12×10^{-5}	9.91×10^{-5}	1.07×10^{-4}
D_{H_2O,S_2} (m^2)	1.42×10^{-4}	1.54×10^{-4}	1.67×10^{-4}
D_{O_2,N_2} (m^2)	1.8×10^{-4}	1.96×10^{-4}	2.12×10^{-4}
D_{K,H_2S} (m^2)	1.06×10^{-3}	1.09×10^{-3}	1.12×10^{-3}
D_{K,H_2O} (m^2)	1.46×10^{-3}	1.50×10^{-3}	1.53×10^{-3}
D_{K,S_2} (m^2)	7.76×10^{-4}	7.94×10^{-4}	8.13×10^{-4}
D_{K,O_2} (m^2)	1.1×10^{-3}	1.12×10^{-3}	1.15×10^{-3}
μ_{air} (kg (m s)$^{-1}$)	3.71×10^{-5}	3.82×10^{-5}	3.93×10^{-5}
μ_{fuel} (kg (m s)$^{-1}$)	3.7×10^{-5}	3.85×10^{-5}	4.01×10^{-5}
$\Delta\phi_c^0$ (V)	0.886	0.880	0.872
σ_a ((Ω m)$^{-1}$)	13.1	9.88	5.26
σ_c ((Ω m)$^{-1}$)	1.11×10^6	1.06×10^6	1.02×10^6
σ_m ((Ω m)$^{-1}$)	1.49	2.39	3.66
$[\sigma/l]_{contact}$ (Ω^{-1} m^{-2})	7670	7000	7730

method minimizes the sum of the squares of the difference between experimental data points and the model output by varying the parameters to be estimated.

The data are filtered before being sent to the estimation algorithm. This filtering includes:

(1) The *i–V* data are smoothed to remove noise. The Robust Lowess smoothing method provided in MATLAB's Curve Fitting Toolbox was used [32].
(2) Repeating data points and data values against the trend are removed.
(3) Current density values are interpolated for an equally spaced vector of voltage values to get a *i–V* matrix of a manageable size. For all four models used in this study, the **V** vector was defined by 16 equally spaced points that went from 99% of the open circuit potential of the cell to 0 V.

The parameter estimation routine takes this matrix of *i–V* data at each temperature and uses the models to iterate to i_0 values that fit the given data best. The 1-D explicit model calculates the cell voltage as a function of specified average current density while the 1-D implicit and the 2-D models calculate current density for a specified cell operating voltage. Thus, the parameter estimation needs to be set up differently depending on the model being fitted.

3.1. Mathematical formulation for 1-D explicit model

$$\min_{i_a^0, i_c^0} \sum_{k=1}^{n} \{V_m(i_k, T) - V_{k,T}\}^2$$
$$\text{subject to :} \tag{59}$$
$$V_m = f(i, T, i_a^0, i_c^0, \mathbf{p})$$

where $V_m(i_k,T)$ is the output cell voltage given by the model for the current density i_k while $V_{k,T}$ is the experimentally observed cell voltage at current density i_k. The vector **p** represents the known parameters (e.g., σ_j, $D_{j,\text{eff}}$) needed to solve the model for V_m, and n is the number of data points.

3.2. Mathematical formulation for 1-D implicit and 2-D models

$$\min_{i_a^0, i_c^0} \sum_{k=1}^{n} \{i_m(V_k, T) - i_{k,T}\}^2$$
$$\text{subject to :} \tag{60}$$
$$i_m = g(V, T, i_a^0, i_c^0, \mathbf{p}^*)$$

where $i_m(V_k,T)$ is the output cell current density given by the model for a cell voltage of V_k and $i_{k,T}$ is the experimentally observed current density for the same cell voltage of V_k. The vector **p***, again represents the known parameters needed to solve the model for i_m.

3.3. Computational resources used

All parameter estimation routines were run using the function *lsqnonlin* in the MATLAB Optimization Toolbox [31]. The 1-D explicit model's parameter estimation took ≈1 s on a 3 GHz Intel Pentium computer. The 1-D implicit model's parameter estimation took ≈5 min while parameter estimation for the 2-D models took from 5 to 14 h per data set. As seen in the section on modelling, the 1-D explicit model calculates the output $V_m(i)$ as an explicit function of *i,* while the 1-D implicit model needs to solve a system of 6 coupled non-linear algebraic equations to calculate $i_m(V)$. For the 2-D models presented here, COMSOL Multiphysics solves for ≈30,000 degrees of freedom to calculate the current drawn by the cell at a given cell voltage.

4. Results and discussion

The results of the parameter estimation for all four models are summarized in Table 3. The last column on the right hand side gives the scaled fit for all the models at the three temperatures. These numbers are obtained by scaling the normalized fit with the maximum value in the data being fitted: $\sqrt{(\sum (V_m - V_k)^2/n)}/(\max(V_k))$ for the 1-D explicit model and $\sqrt{(\sum (i_m - i_k)^2/n)}/(\max(i_k))$ for the other two models.

There are several trends that can be discerned from this data. The first one is that i_a^0 and i_c^0 increase with increasing temperature for all the models. This trend is expected for catalyzed electrochemical reactions.

Model fit to data improves with increasing temperature for all the models. The models fit the data at 850 °C better than at 800 and 750 °C (see Figs. 2–4). A simplistic explanation for this trend is that the performance curves become less non-linear and thus easier to fit, with increasing temperature. However, the models do allow a non-linear *i–V* response through the electrochemical rate equations Eqs. (52) and (53). We believe this mismatch, more severe at lower temperatures due to the lower i_j^0, is related to the symmetric charge transfer coefficients ($2(1-\beta)$ and 2β with $\beta = 0.5$) used in the electrochemical rate equations. These values are obtained by assuming a reaction

Table 3
Parameter estimation results

Model used	T (°C)	i_a^0 (A m^{-2})	i_c^0 (A m^{-2})	Scaled fit
1-D explicit	750	70.0	70.0	2.85×10^{-2}
	800	180.7	180.6	1.50×10^{-2}
	850	344.9	344.9	3.98×10^{-3}
1-D implicit	750	60.1	62.3	4.14×10^{-2}
	800	157.5	163.3	2.15×10^{-2}
	850	300.0	309.1	9.32×10^{-3}
2-D Fickian mass transfer	750	55.0	73.3	4.14×10^{-2}
	800	181.7	187.2	2.51×10^{-2}
	850	571.1	356.3	1.59×10^{-2}
2-D Maxwell–Stefan mass transfer	750	54.1	74.5	4.13×10^{-2}
	800	163.9	199.3	2.50×10^{-2}
	850	565.8	362.9	1.60×10^{-2}

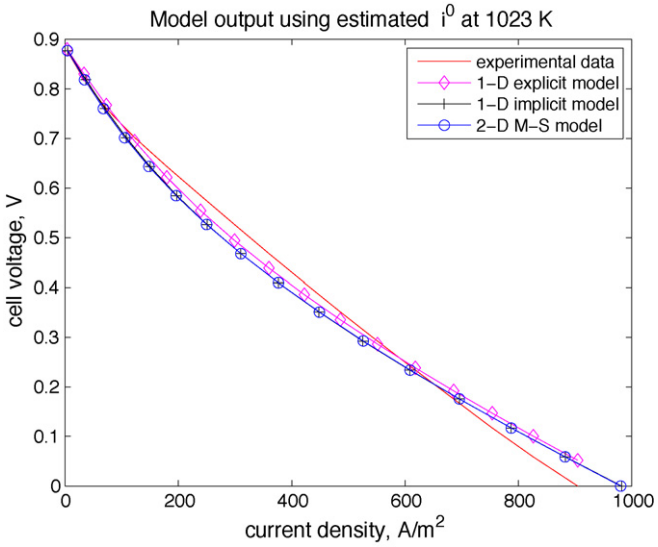

Fig. 2. Model output using optimized i^0 at 750 °C.

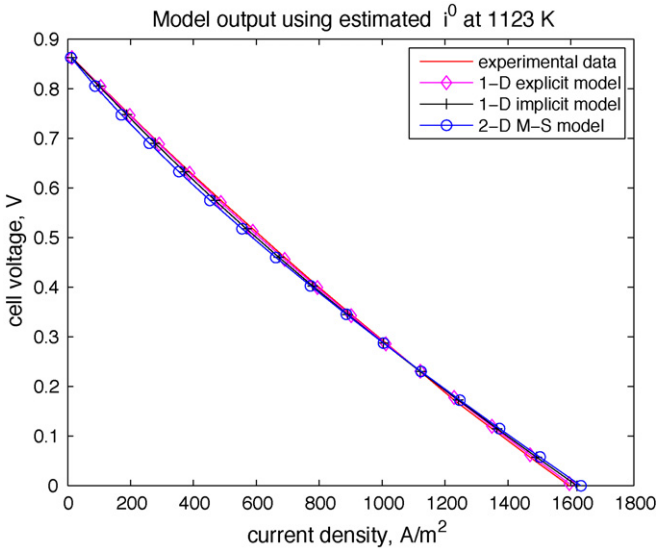

Fig. 4. Model output using i^0 at 850 °C.

mechanism with a rate controlling two electron transfer step. Ongoing research in our group is focussing on deriving better electrochemical rate equations.

According to the scaled fit values in Table 3 the 1-D explicit model seems to give a better fit to the data at all three temperatures. It does seem counterintuitive that a model that we know to be too simple to explain all that is happening in the fuel cell gives a better fit to the experimental data. However, visual examination of the model fit for the different models to the experimental *i–V* data does not show any significant difference between the fit for the 1-D versus 2-D models, and as we note later, the 1-D models cannot correctly calculate the coupled activation and concentration losses, especially at the low flow-rates used here.

All models give values for i_a^0 and i_c^0 that give a fair Arrhenius temperature dependence. The Arrhenius plot for the i_a^0 and i_c^0 given by the 2-D model using Maxwell–Stefan mass transfer is

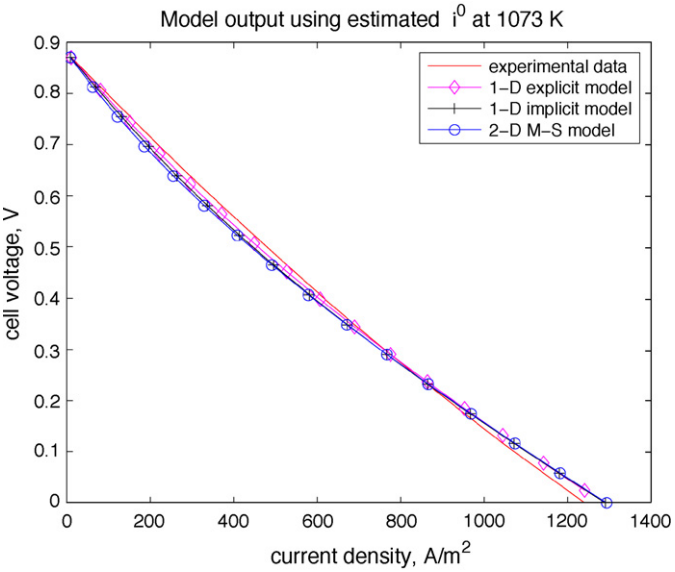

Fig. 3. Model output using optimized i^0 at 800 °C.

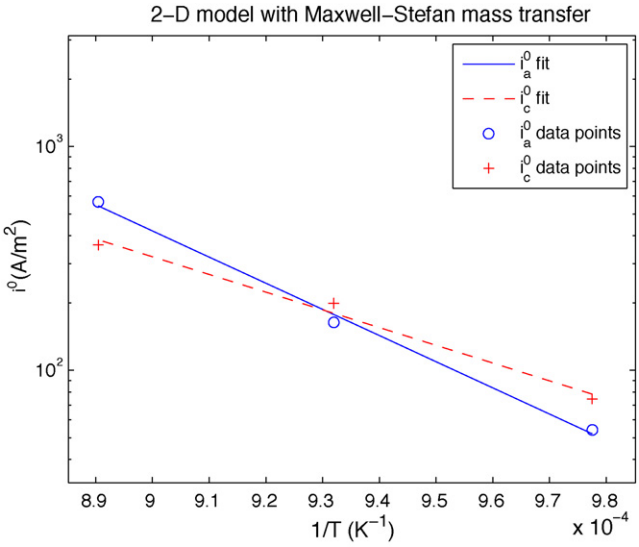

Fig. 5. Arrhenius plot for i^0 from 2-D M–S model.

shown in Fig. 5. This plot gives the i^0 versus $1/T$ curves obtained with pre-exponentials and activation energies calculated using the optimal i_a^0 and i_c^0. The plot also shows the actual optimal values for the exchange current densities used to calculate the least squares fitted values for A_j and E_j in Eq. (61). These pre-exponential factors and activation energies are given in Table 4:

$$i_a^0 = A_a e^{-E_a/RT}$$
$$i_c^0 = A_c e^{-E_c/RT} \quad (61)$$

Table 4
Arrhenius parameters estimated for i^0 in 2-D Maxwell–Stefan model

	i_a^0	i_c^0
A (A m^{-2})	1.41×10^{13}	4.35×10^{9}
E (kJ mole^{-1})	224	152

4.1. The 1-D models

The main difference between the 1-D explicit and the 1-D implicit models is that in the explicit model the reaction rate is independent of the local species concentrations (Eqs. (5) and (6)) whereas the reaction rate in the implicit model depends on the local concentrations at the reaction surface (Eqs. (20) and (21)). In the implicit model the reaction rate is thus coupled to the mass transfer whereas the activation and concentration losses are decoupled and separable in the explicit model. The above difference between the two models, however, gives no clear indication as to how it would affect i^0 estimates.

4.2. 1-D implicit model versus 2-D Fick model

For all the three data sets or temperatures, the i^0 values in the 1-D implicit model are lower than those in the 2-D model using Fick mass transfer. This difference can be explained by the difference in species concentrations at the interface between the electrodes and the electrolyte in the two models. The 2-D model accounts for flow and mass transfer in the gas channels and is thus able to include the mass transfer resistance in the flow domain. The 1-D implicit model cannot account for the inherently two-dimensional flow field in a button cell and cannot account for mass transfer in the channels correctly. Therefore, the parameter estimation for the 1-D implicit model ends up assigning a higher activation resistance (lower i^0). A plot of the mass fraction profile of O_2 along the axis of the cell is given in Fig. 6. This supports the above discussion by illustrating the difference between the 1-D and 2-D models in predicting concentrations at the cathode–electrolyte boundary (surface where the cathode reaction occurs).

The above discussion also implies that if sufficiently high flow-rates are used, the 1-D implicit model will approximate the 2-D model better. This is verified in Fig. 7 where two i–V curves

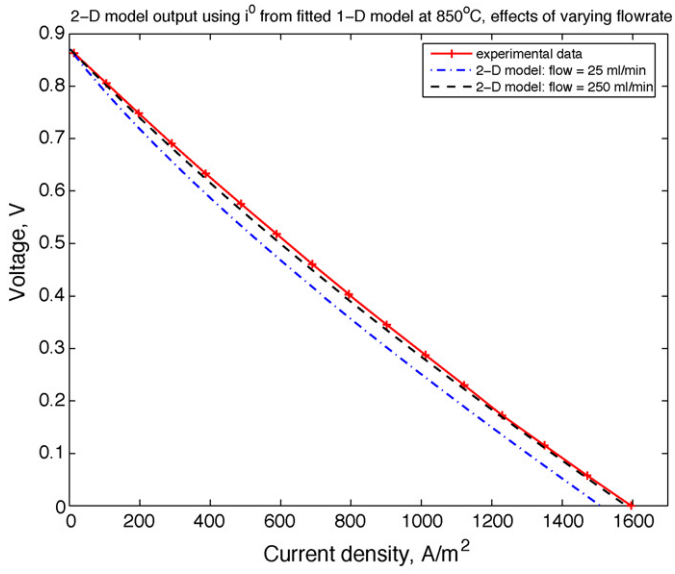

Fig. 7. 2-D model output using i^0 from 1-D model at 850 °C at different flow-rates.

generated using the 2-D Maxwell–Stefan model are compared to the experimental data at 850 °C. The two curves given have the same values for i_a^0 and i_c^0: the parameter estimates for the 1-D implicit model. The flow-rates of the gas streams, however, are 25 ml min^{-1} for one curve and 250 ml min^{-1} for the other. As clearly seen in Fig. 7, the model output for the higher flow-rate is able to approximate the experimental data quite well even though the kinetic parameters used are obtained from the 1-D model. This is because the higher flow-rate dramatically decreases the mass transfer resistance in the gas channels.

The radial variation of species concentrations is insignificant as seen in Fig. 8. The rise in w_{O_2} from the left to the right of Fig. 8 is due to diffusion into the electrode from the electrode edge at the right.

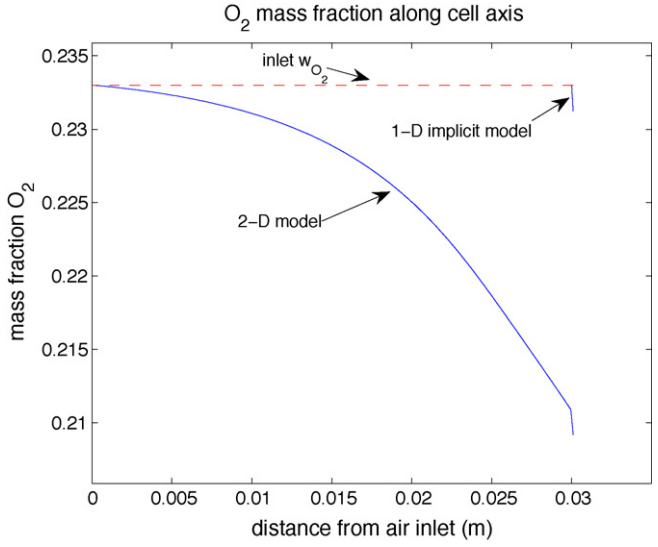

Fig. 6. O_2 mass fraction profiles along axis for the 1-D implicit and 2-D models at 850 °C.

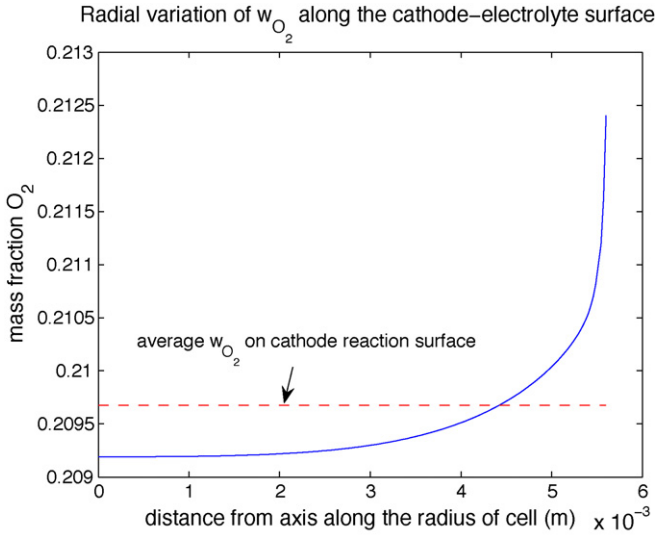

Fig. 8. O_2 mass fraction radial profile in the 2-D Maxwell–Stefan model at 850 °C.

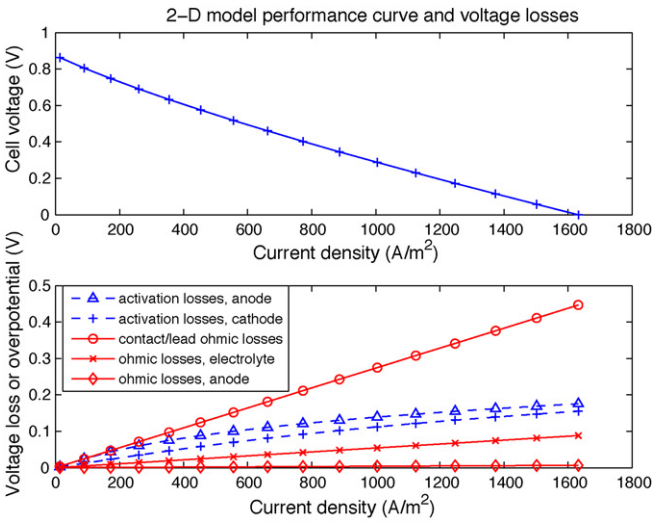

Fig. 9. Voltage loss profiles in the 2-D Maxwell–Stefan model at 850 °C.

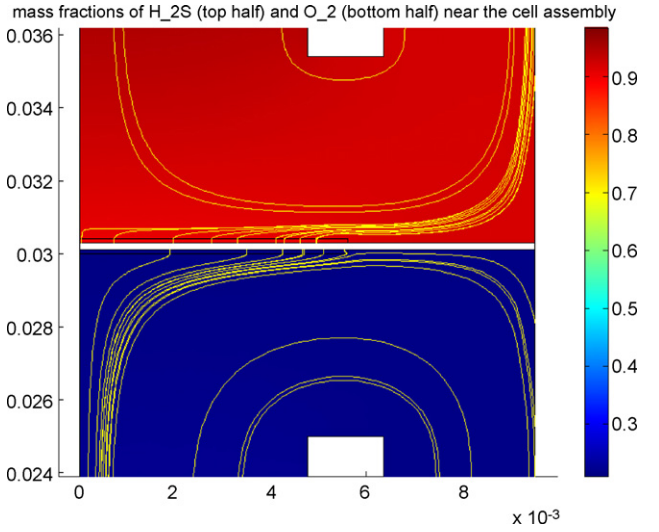

Fig. 10. Mass fraction profiles of the reactants in the 2-D Maxwell–Stefan model at 0 V, 850 °C.

4.3. The 2-D models

The 2-D models used differ only in how they compute the mass transfer of the different species. The Maxwell–Stefan mass transfer formulation is superior to the Fick mass transfer form because it correctly accounts for the variation in the diffusivites of the different components with composition [33].

Taking the 2-D model with Maxwell–Stefan mass transfer to be the most faithful model, we now discuss the profiles of the different voltage losses in the SOFC. Fig. 9 gives the cell voltage as well as various voltage losses (commonly called overpotentials) as a function of cell current density according to the second 2-D model at 850 °C.

The plot clearly shows that the highest voltage loss is due to the contact/current lead resistances which account for 2.68 Ω or 80% of the total ohmic resistance of 3.33 Ω at 850 °C. The anodic and cathodic activation losses, respectively, are next highest, followed by the ohmic loss in the electrolyte. The ohmic loss in the anode is roughly 14 times smaller than the ohmic loss in the electrolyte, while that in the cathode is another 4 orders of magnitude smaller than in the anode. The relative magnitudes of the different ohmic losses can also be readily calculated from the resistivity values and the breadths of the different phases (Tables 1 and 2).

Fig. 10 gives the mass fractions of the reactants near the electrode–electrolyte assembly in the modelled SOFC at an operating voltage of 0 V (short-circuited cell drawing maximum current). The vertical boundary on the left is the axis of symmetry of the cell, the gap in the middle is the electrolyte, and the top half is the fuel side while the bottom half the air side. The mass fraction of H_2S on the fuel side and the mass fraction of O_2 on the air side is shown using a colour scale given on the right hand side of the figure. As readily apparent, even at maximum current, the cell operating conditions are well away from the reactant starved regime where what are normally termed concentration losses become dominant. The streamlines for the flow in the channels and the electrodes are also plotted in Fig. 10 and show the flow turning around after hitting the electrodes. The streamlines enter the electrolyte at the cathode and appear at the anode electrolyte boundary to show how the oxygen is transported across the cell from the cathode through the electrolyte to the anode, where it comes out as H_2O.

5. Conclusions and future work

The primary ongoing goal of this work is to build a mathematical model for the single H_2S SOFC cell that can then be used to help in further development of H_2S fuelled cells or stacks. Four models of increasing complexity have been presented and compared for a button cell SOFC fuelled by H_2S. Non-linear least squares were used to estimate the unknown electrochemical kinetic parameters for all the models. Examination of these parameter estimates, and the fit between the model output and experimental data used, allows us to identify expected patterns in the parameters and compare the four models and their ability to simulate SOFC operation. We suggest the 2-D model with Maxwell–Stefan mass transfer be used in further modelling studies because it is the one that accounts for the mass transfer resistance and thus the activation resistance accurately, and is the most comprehensive of the four models presented here.

To comprehensively validate these models, reliable estimates for the exchange current densities from electrode characterization studies are needed. Detailed electrochemical studies of the electrodes should also throw some light on the actual reaction mechanisms and hopefully yield better rate expressions. In fact, given enough information about the experimental setup, our models can be modified to simulate the electrochemical characterization experiments.

We believe that the biggest shortcoming of our model is that the reaction mechanisms used to derive the rate expressions are too simplistic. One of the next steps in our work will be to propose more complex reaction models that include multiple elementary reaction steps at each electrode as well as competitive adsorption and desorption of reaction species. The rate expres-

sions derived for the above mechanisms can then be included in our models and should lead to better matches to experimental cell performance data. These rate equations, however, typically have more kinetic parameters than just the exchange current densities. To get reliable estimates for these kinetic parameters and to validate any proposed reaction mechanisms, very careful experimental characterization of the electrodes using half cell experiments [34,35] is required.

Another possible approach to get at electrode reaction mechanisms and rate equations is through molecular modelling. Methods from theoretical chemistry such as density functional theory, which are based on a quantum mechanical description of the bonds between atoms, can be used to find feasible electrode reaction mechanisms [36,37]. These methods can also give estimates for the kinetic parameters for the elementary reactions in a given reaction mechanism [38]. Sun et al. [39] have used the above approach to investigate the hydrodesulfurization (HDS) reaction on MoS_2, NiMoS, and CoMoS. In the HDS reaction, H_2 is used to remove S from the sulfided surface, while in a H_2S SOFC anode, H_2S adsorbs and dissociates on the surface. The H (and perhaps the S) atoms near the anode–electrolyte interface then presumably react with oxide ions in the electrolyte to give reaction products. In future work, we propose to use results from the approach outlined here to build a better model for the electrochemistry in the anode.

These updated models will then be used to do parametric studies with variation in fuel composition, flow-rates and temperatures. We also intend to include heat transfer in our model to examine the temperature variations in the operating cell and to check whether a thermally self sustaining SOFC using H_2S is possible.

References

[1] M. Capone, Sulfur removal and recovery, in: Kirk-Othmer Encyclopedia of Chemical Technology Online, fourth ed., John Wiley and Sons, 2004, URL http://www.mrw.interscience.wiley.com/kirk/articles/sulfcapo.a01/sec1_3-fs. html.

[2] N.U. Pujare, K.W. Semkow, A.F. Sammells, A direct H_2S/air solid oxide fuel cell, J. Electrochem. Soc. 134 (1987) 2639–2640.

[3] N.U. Pujare, K.J. Tsai, A.F. Sammells, Electrochemical claus process for sulfur recovery, J. Electrochem. Soc. 136 (1989) 3662–3678.

[4] C. Yates, J. Winnick, Anode materials for a hydrogen sulfide solid oxide fuel cell, J. Electrochem. Soc. 146 (1999) 2841–2844.

[5] M. Liu, P. He, J.L. Luo, A.R. Sanger, K.T. Chuang, Performance of a solid oxide fuel cell utilizing hydrogen sulfide as fuel, J. Power Sources 94 (2001) 20–25.

[6] M. Liu, G. Wei, J. Luo, A.R. Sanger, K.T. Chuang, Use of metal sulfides as anode catalysts in H_2S–air SOFCs, J. Electrochem. Soc. 150 (2003) 1025–1029.

[7] L. Aguilar, S. Zha, Z. Cheng, J. Winnick, M. Liu, A solid oxide fuel cell operating on hydrogen sulfide and sulfur-containing fuels, J. Power Sources 135 (2004) 17–24.

[8] G.L. Wei, M. Liu, J.L. Luo, A.R. Sanger, K.T. Chuang, Influence of gas flow-rate on performance of H_2S–air solid oxide fuel cells with MoS_2–NiS–Ag anode, J. Electrochem. Soc. 150 (2003) 463–469.

[9] G.-L. Wei, J.-L. Luo, A.R. Sanger, K.T. Chuang, L. Zhong, Li_2SO_4-based proton-conducting membrane for H_2S–air fuel cell, J. Power Sources 145 (2005) 1–9.

[10] S.V. Slavov, K.T. Chuang, A.R. Sanger, J.C. Donini, J. Kot, S. Petrovic, Proton-conducting solid state H_2S–O_2 fuel cell. i. Anode catalysts, and operation at atmospheric pressure and 20–90 °C, Int. J. Hydrogen Energy 23 (1998) 1203–1212.

[11] K.T. Chuang, A.R. Sanger, S.V. Slavov, J.C. Donini, A proton-conducting solid state H_2S–O_2 fuel cell. iii. Operation using H_2S–hydrocarbon mixtures as anode feed, Int. J. Hydrogen Energy 26 (2001) 103–108.

[12] D. Peterson, J. Winnick, A hydrogen sulfide fuel cell using a proton-conducting solid electrolyte, J. Electrochem. Soc. 143 (1996) 55–56.

[13] T. Kirk, J. Winnick, A hydrogen sulfide solid-oxide fuel cell using ceria-based electrolytes, J. Electrochem. Soc. 140 (1993) 3494–3496.

[14] G.-L. Wei, J.-L. Luo, A.R. Sanger, K.T. Chuang, High-performance anode for H_2S–air sofcs, J. Electrochem. Soc. 151 (2004) 232–237.

[15] M.A. Khaleel, Z. Lin, P. Singh, W. Surdoval, D. Collin, A finite element analysis modeling tool for solid oxide fuel cell development: coupled electrochemistry, thermal and flow analysis in MARC^{TM}, J. Power Sources 130 (2004) 136–148.

[16] P.G. Debenedetti, C.G. Vayenas, Steady-state analysis of high temperature fuel cells, Chem. Eng. Sci. 38 (1983) 1817–1829.

[17] C.G. Vayenas, P.G. Debenedetti, I. Yentekakis, L.L. Hegedus, Cross-flow, solid-state electrochemical reactors: a steady-state analysis, Ind. Eng. Chem. Fundam. 24 (1985) 316–324.

[18] M.A. Khaleel, J.R. Selman, Cell, stack and system modelling, in: S.C. Singhal, K. Kendall (Eds.), High Temperature Solid Oxide Fuel Cells: Fundamentals, Design and Applications, Elsevier Advanced Technology, Oxford, 2003, pp. 291–331.

[19] S.B. Adler, Factors governing oxygen reduction in solid oxide fuel cell cathodes, Chem. Rev. 104 (2004) 4791–4843.

[20] The Mathworks, Getting Started with MATLAB: Version 7, The Mathworks Inc., Natick, MA, 2005, URL http://www.mathworks.com/products/matlab/.

[21] COMSOL, COMSOL Multiphysics 3.2 User's Guide, COMSOL AB, Sweden, 2005, URL http://comsol.com/products/multiphysics/.

[22] K.B. Oldham, J.C. Myland, Fundamentals of Electrochemical Science, Academic Press, San Diego, 1994.

[23] J.-W. Kim, A.V. Virkar, K.-Z. Fung, K. Mehta, S.C. Singhal, Polarization effects in intermediate temperature, anode-supported solid oxide fuel cells, J. Electrochem. Soc. 146 (1999) 69–78.

[24] S.H. Chan, K.A. Khor, Z.T. Xia, Complete polarization model of a solid oxide fuel cell and its sensitivity to the change of cell component thickness, J. Power Sources 93 (2001) 130–140.

[25] R.B. Bird, W.E. Stewart, E.N. Lightfoot, Transport Phenomena, second ed., John Wiley & Sons, NY, USA, 2002.

[26] R.C. Reid, J.M. Prausnitz, B.E. Poling, The Properties of Gases and Liquids, fourth ed., McGraw-Hill, NY, 1987.

[27] R. Saeger, L. Scriven, H. Davis, Transport processes in periodic porous media, J. Fluid Mech. 299 (1995) 1–15.

[28] M. Liu, Hydrogen sulfide powered solid oxide fuel cells, Ph.D. Thesis, University of Alberta, Edmonton, Canada, 2004.

[29] H.T. Davis, L.R. Valencourt, C.E. Johnson, Transport processes in composite media, J. Am. Ceram. Soc. 58 (9–10) (1975) 446–452.

[30] S. Ahmed, C. McPheeters, R. Kumar, Thermal–hydraulic model of a monolithic solid oxide fuel cell, J. Electrochem. Soc. 138 (1991) 2712–2718.

[31] The Mathworks, Optimization Toolbox User's Guide: Version 3, The Mathworks Inc., Natick, MA, 2004.

[32] The Mathworks, Curve Fitting Toolbox User's Guide: Version 1, The Mathworks Inc., Natick, MA, 2004.

[33] R. Taylor, R. Krishna, Multicomponent Mass Transfer, John Wiley & Sons, NY, USA, 1993.

[34] B. de Boer, Sofc anodes: hydrogen oxidation at porous nickel and nickel/yttria-stabilised zirconia cermet electrodes, Ph.D. Thesis, Universiteit Twente, The Netherlands, 1998.

[35] A.C. Co, Oxygen reduction kinetics and mechanism in high temperature solid oxide fuel cells, Ph.D. Thesis, University of Calgary, Canada, 2005.

[36] M. Neurock, Applications: catalysis, in: WTEC Panel on Applications of Molecular and Materials Modeling, International Technology Research Institute, Kluwer Academic, Baltimore, MD, 2002, pp. 77–106.
[37] T. Ziegler, J. Autschbach, Theoretical methods of potential use for studies of inorganic reaction mechanisms, Chem. Rev. 105 (2005) 2695–2722.
[38] D.G. Truhlar, K. Morokuma (Eds.), Transition State Modeling for Catalysis, ACS Symposium Series 721, American Chemical Society, Washington, DC, 1999.
[39] M. Sun, A.E. Nelson, J. Adjaye, Ab initio DFT study of hydrogen dissociation on MoS_2, NiMoS, and CoMoS: mechanism, kinetics, and vibrational frequencies, J. Catal. 233 (2005) 411–421.